PNAS
www.pnas.org

Supplementary Information for

Understanding cytoskeletal avalanches using mechanical stability analysis

Carlos Floyd, Herbert Levine, Christopher Jarzynski, Garegin A. Papoian

Corresponding Authors: Christopher Jarzynski and Garegin A. Papoian.
E-mail: cjarzyns@umd.edu and gpapoian@umd.edu

This PDF file includes:

Supplementary text
Figs. S1 to S14 (not allowed for Brief Reports)
Table S1 (not allowed for Brief Reports)
Legends for Movies S1 to S5
SI References

Other supplementary materials for this manuscript include the following:

Movies S1 to S5

Supporting Information Text

1. Supplementary Figures

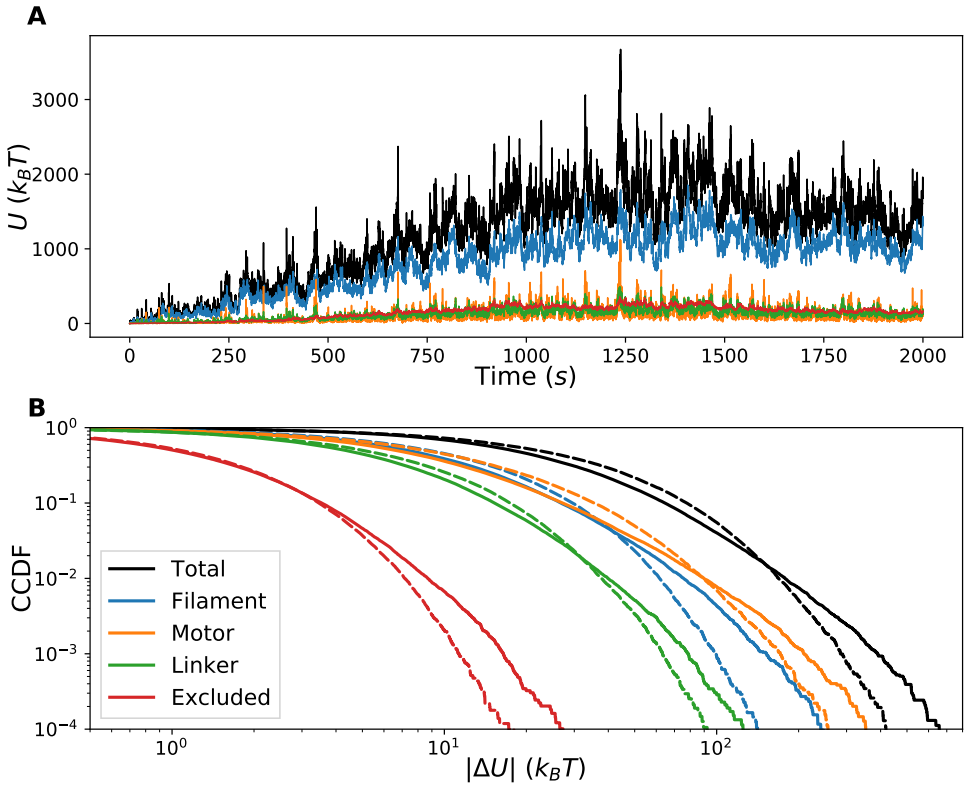

Fig. S1. The decomposition of the total mechanical energy U into contributions from the molecular components of the cytoskeletal network. These contributions include stretching and bending of actin filaments, stretching of myosin motors, stretching of cross-linkers, and the excluded volume repulsion between nearby actin filaments (see SI Appendix, Description of MEDYAN simulation platform for further details on the network's mechanical potential). **A**: The trajectory of each component's energy over time is shown, corresponding to the plot shown in Figure 1.A of the main text. The colors of each line are described in the legend of the bottom panel. **B**: The complementary cumulative distribution functions for positive (solid lines) and negative (dashed lines) increments of each component are shown. This corresponds to Figure 1.B of the main text. All distributions are heavy tailed ($\eta_{\pm} > 0$, where η_- describes $|\Delta U_-|$ and η_+ describes ΔU_+ for each component) and asymmetric, with heavier tails for negative increments ($\eta_- > \eta_+$). These plots show that at any time, most of the energy of the network is stored in the filament strain energy, but the changes in mechanical energy of myosin motors and actin filaments are comparable.

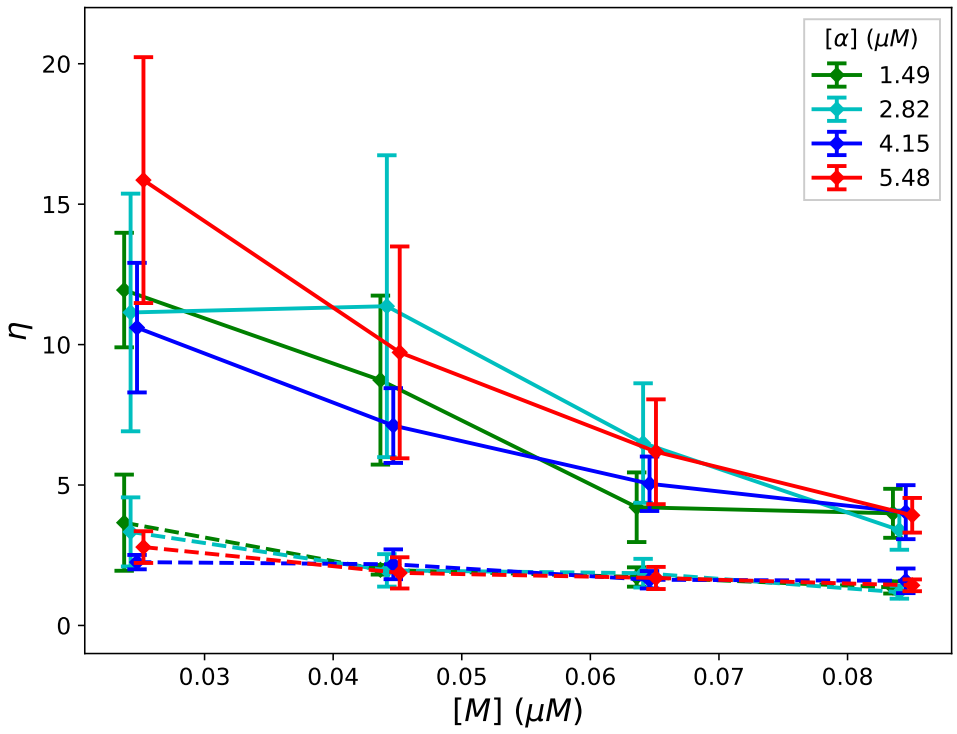

Fig. S2. Plots of the non-Gaussian parameter η for the distributions of $|\Delta U_-|$ (solid lines) and of ΔU_+ (dashed lines) at QSS for various concentrations of myosin motor ($[M]$) and α-actinin cross-linkers ($[\alpha]$). The mean and standard deviation is shown over five runs of each condition. A small horizontal offset is added to the points to ease visibility.

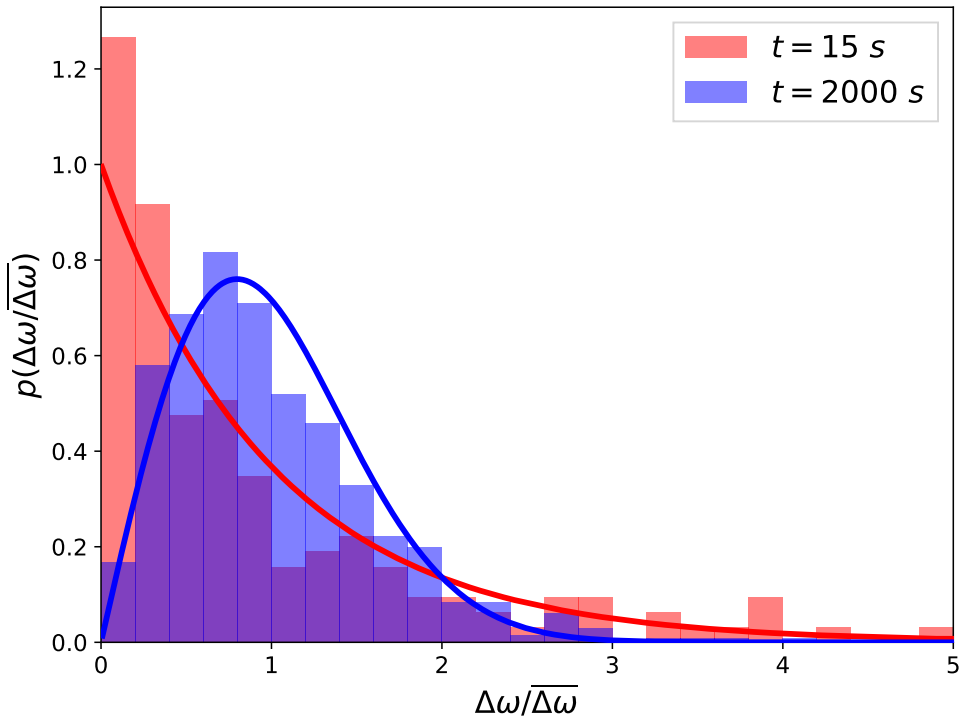

Fig. S3. Histograms of the level spacings $\Delta\omega = \omega_{k+1} - \omega_k$, where $\omega_k = \sqrt{\lambda_k}$ are ordered so that ω_k increases as k increases, normalized by their average $\overline{\Delta\omega}$ for the very soft ($\lambda_k < 10\ pN/nm$) and delocalized ($r_k > 100$) vibrational modes at different times of a run of condition $C_{3,3}$. The Poisson distribution $p(\Delta\omega/\overline{\Delta\omega}) = e^{-\Delta\omega/\overline{\Delta\omega}}$ and the Wigner-Dyson distribution $p(\Delta\omega/\overline{\Delta\omega}) = \frac{\pi}{2}(\Delta\omega/\overline{\Delta\omega})e^{-\frac{\pi}{4}(\Delta\omega/\overline{\Delta\omega})^2}$ are plotted as red and blue solid lines. This transition in distributions signifies that in the percolated network at $2000\ s$ the frequencies of these modes are no longer randomly spaced and begin to interact, exhibiting level repulsion for small $\Delta\omega/\overline{\Delta\omega}$.

2. Weibull plots

The degree to which the plots of $Q(u) = \ln(-\ln(P(x \geq u)))$ against $\ln(u)$ appear to be linear serves as a check of the appropriateness of modeling $P(x)$ as a stretched exponential, or Weibull, distribution (1). See Figure S4 for $x = |\Delta U -|$ and Figure S5 for $x = \Delta U_+$. On the basis of these plots we conclude that the Weibull distribution is a satisfactory choice for all values of V. In the main text, the Weibull parameters k and λ were determined by fitting the stretched exponent $e^{-(x/\lambda)^k}$ to the observed CCDF $P(|\Delta U_-|)$ on a log-scale, that is, by fitting $-(x/\lambda)^k$ to $\ln(P(|\Delta U_-|))$ using standard nonlinear fitting routines. Treating these functions on a log-scale ensured a better fit to the distribution tails which are of most interest in the present case.

We interpret these fits to a Weibull distribution as mainly empirical, rather than as representing a "true" description of the distribution of ΔU. We could view the true distribution as being constructed by drawing samples from the distributions for each contribution to the total energy of the network's molecular components and summing them together (see SI Appendix, Figure S1). ΔU would be distributed as a convolution over these underlying distributions if the samples were drawn independently, but we expect them to instead be dependent. Rather than attempt to build up a model for the distribution ΔU from these underlying distributions, here we directly fit Weibull distributions which allows us to straightforwardly parameterize the distribution and study its scaling with system volume (see Figure 5 of the main text). Building a multicomponent statistical model for the distribution of ΔU would be an interesting direction for future work, however.

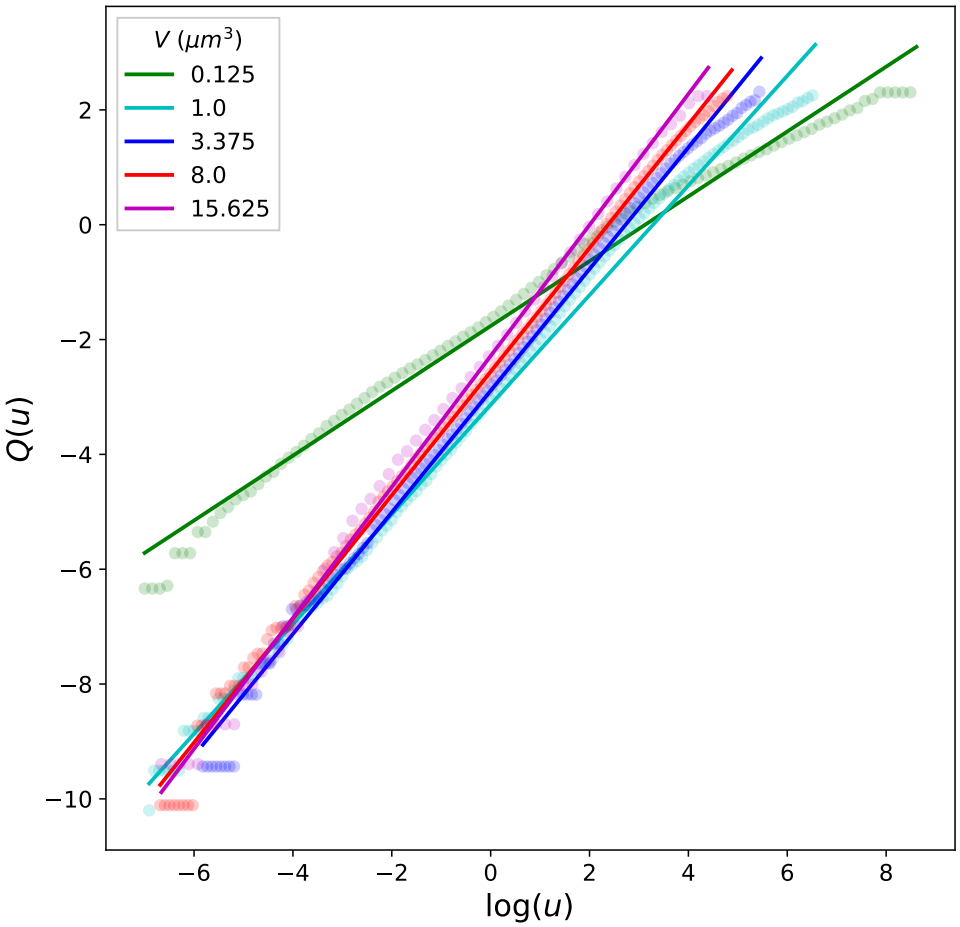

Fig. S4. Plots of the function $Q(u) = \ln(-\ln(P(|\Delta U_-| \geq u)))$ for different volumes V along with a fitted line, where $P(|\Delta U_-|)$ is the observed CCDF obtained from five runs of each volume.

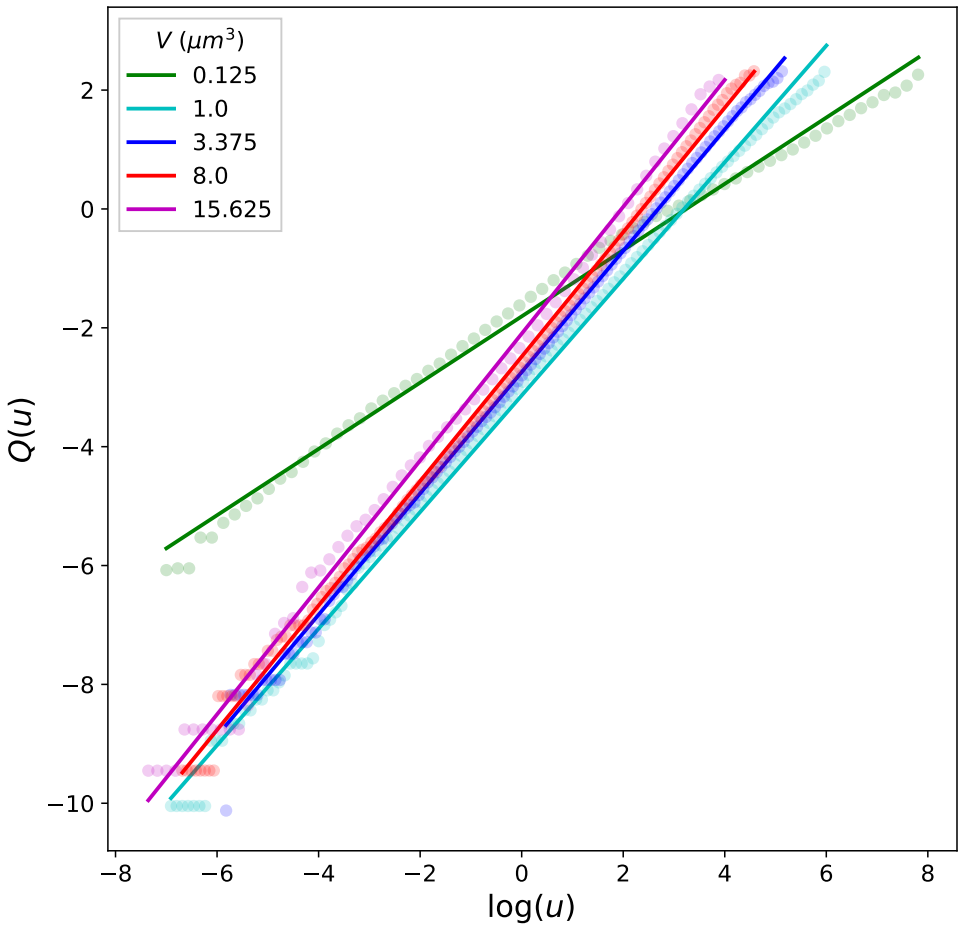

Fig. S5. Plots of the function $Q(u) = \ln(-\ln(P(\Delta U_+ \geq u)))$ for different volumes V along with a fitted line, where $P(\Delta U_+)$ is the observed CCDF obtained from five runs of each volume.

3. Filament displacements

The area between the two filaments $\mathbf{x}$ and $\mathbf{y}$ is triangulated using the beads comprising the filaments ($\{\mathbf{x}_i\}_{i=0}^{n_\mathbf{x}-1}$ and $\{\mathbf{y}_j\}_{j=0}^{n_\mathbf{y}-1}$) as vertices, where $n_\mathbf{x}$ is the number of beads in $\mathbf{x}$ and similarly for $n_\mathbf{y}$. To compute the displacement of filament $\mathbf{x}$ during the time interval δt, we set $\mathbf{y}$ to the new configuration of $\mathbf{x}$ at the end of the interval. The triangles come in pairs for most of the filament lengths, as shown using the dark and light colors of green of Figure S6. If $n_\mathbf{x}$ and $n_\mathbf{y}$ are unequal (say $n_\mathbf{x} < n_\mathbf{y}$), extra triangles are added using the last bead in $\mathbf{x}$, $\mathbf{x}_{n_\mathbf{x}-1}$, as the only vertex in filament $\mathbf{x}$. The sum of these triangle areas A_{tot} is divided by the average of the two filament contour lengths $L_\mathbf{x}$ and $L_\mathbf{y}$ to give the measure of distance $d = \frac{2A_{\text{tot}}}{L_\mathbf{x}+L_\mathbf{y}}$.

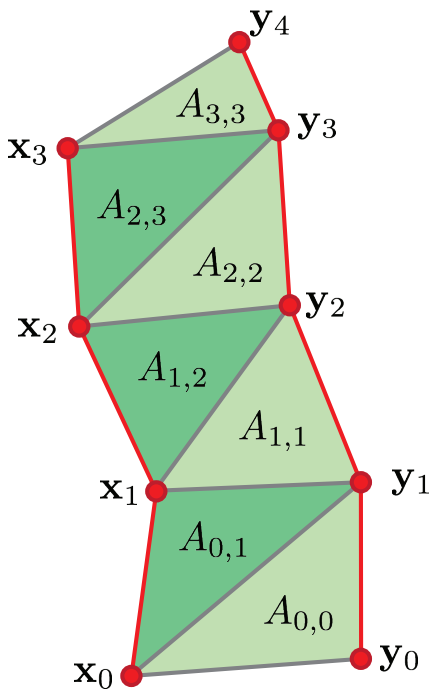

Fig. S6. Illustration of how the area between two filaments $\mathbf{x}$ and $\mathbf{y}$ is triangulated to allow calculation of the distance between them. The beads comprising the filaments are labeled $\mathbf{x}_i$, $\mathbf{y}_j$, and areas between triplets of beads are labeled $A_{i,j}$ where the lowest indices of the beads $\mathbf{x}_i$ and $\mathbf{y}_j$ in the triplet are used.

4. Binning

One goal of our study is to explore the correlations between anomalous changes in the network's mechanical energy ΔU and other measures of network dynamics, including the filament displacements, numbers of motor walking events and cross-linker unbinding events, the change in the spatial uniformity of tension (see Figure 3 of the main text), and the effective stiffness of the network motion (see Figure 8 of the main text). To this end, the joint distributions of these pairs of quantities are constructed at quasi-steady state. One difficulty in dealing directly with the full joint distributions to study anomalous events is the concentration of probability around $\Delta U = 0\ k_BT$ (see Figure S7). Measures of correlation defined on the full numerical data, such as the maximal information criterion, will provide information mainly about the bulk of data around $\Delta U = 0\ k_BT$ rather than about the tails which we are interested in (2). To facilitate studying correlations in the tails of the distribution of ΔU, we convert the numerical values of ΔU to categorical labels via binning and compare the distributions of other network measures between these bins using statistical tests such as Kruskal-Willis and the Wilcoxon rank sum test (3). The bins near $\Delta U = 0\ k_BT$ contain more data than those near the tails, but these statistical tests are still valid on groups with different numbers of samples. In the main text, results based on these statistical tests are reported using four bins with edges at $-\infty,\ -100,\ 0, 100$, and $\infty\ k_BT$. These bins represent both negative and positive values of ΔU as well as typical and atypical magnitudes of ΔU. One can ask whether our main results are sensitive to the choice of bins edges or the number of bins. This was tested by varying the lowest bin edge from -300 to $-50\ k_BT$ (keeping the even total number of bins distributed symmetrically about $\Delta U = 0\ k_BT$), and varying the total number of uniformly spaced bins (excluding those with edges at $\pm\infty$) from 4 to 10. Our primary conclusions in the main text, that there is a significant difference between any of the bins and that the bins near the lower tail of ΔU have extremal typical values of the correlated network measures, were found not to be sensitive to these different choices for bins. In each case there were statistically significant test results that agree with the conclusions reported in the main text.

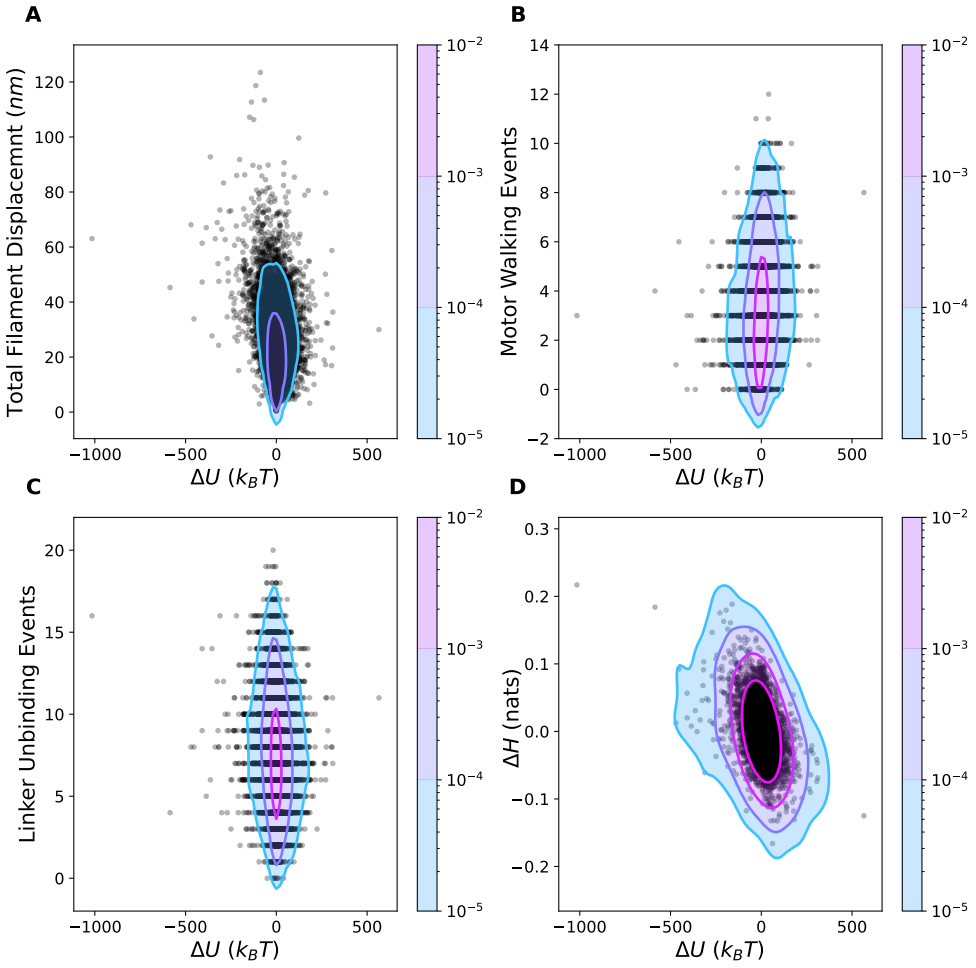

Fig. S7. The scatter plot data at quasi-steady state from which Figure 3 in the main text is constructed via binning with respect to ΔU. For each panel a Gaussian kernel density estimate of the joint probability density function is constructed and shown as a contour plot. The labels of the contour are the values of the density function (c.f. Figure 8 in the main text).

5. Degree distributions

One may ask whether the connectivity of the network itself, viewed as a graph object as described in the main text, is at a critical point and whether this may explain the observed heavy-tailed distributions of mechanical energy fluctuations. Previous studies have indicated a tendency for actomyosin networks in 2D to self-organize to a critically connected architecture similar to the onset of percolation, and this tendency was observed to be robust against modest changes in the concentration of cross-linking proteins (4). To investigate whether our data can be explained by critically connected network architectures, we plot the distributions of the weighted node degree (i.e. how many linkers are bound to each filament, Figure S8) in the network and the node connectivity (i.e. how many filaments would have to be removed to disconnect a given pair of filaments, Figure S9) across the tested range of conditions of cross-linker and motor concentrations $C_{i,j}$ (see the Materials and Methods for a description of the experimental conditions). The absence of power laws in these plots indicate that the networks are not critically connected, lying for most conditions well above the percolation threshold.

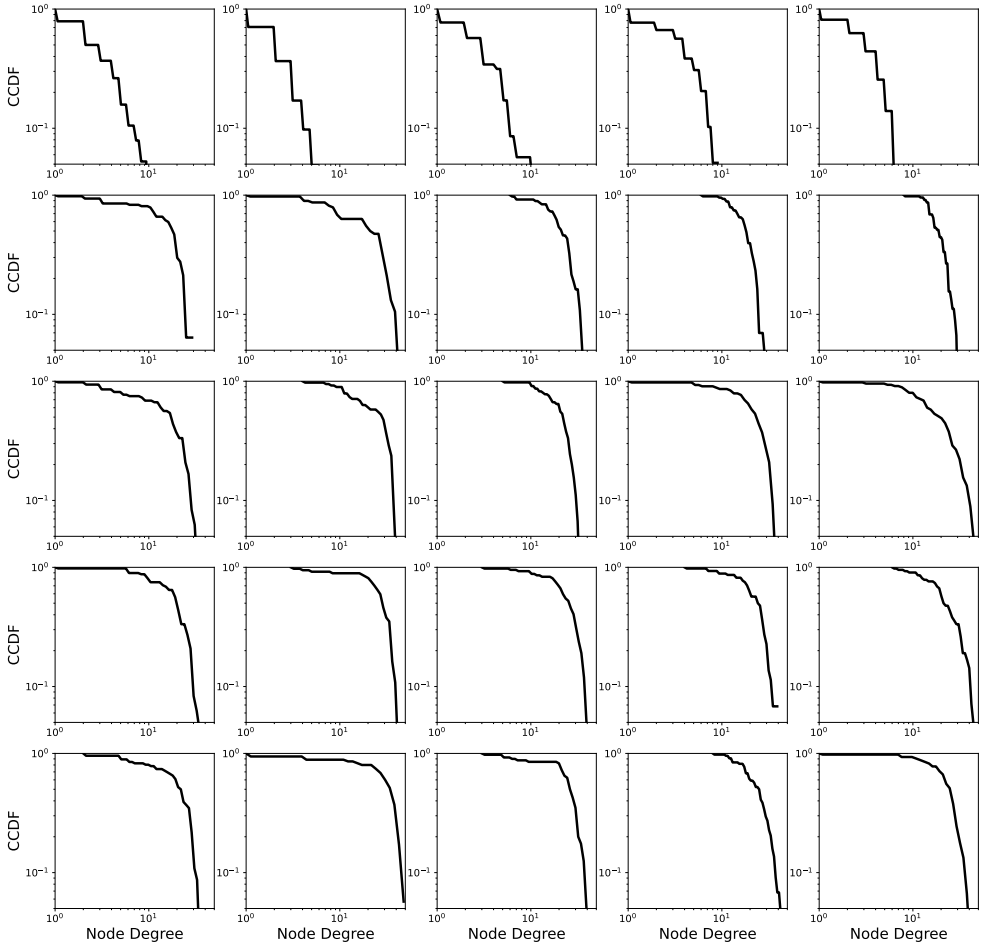

Fig. S8. The weighted degree distributions for networks of each condition $C_{i,j}$, where i (j) indexes the row (column) of the corresponding plot in the grid. These plots are constructed from a single snapshot at quasi-steady state from a trial of each condition. The lack of power laws in these plots indicate that the networks are not critically connected.

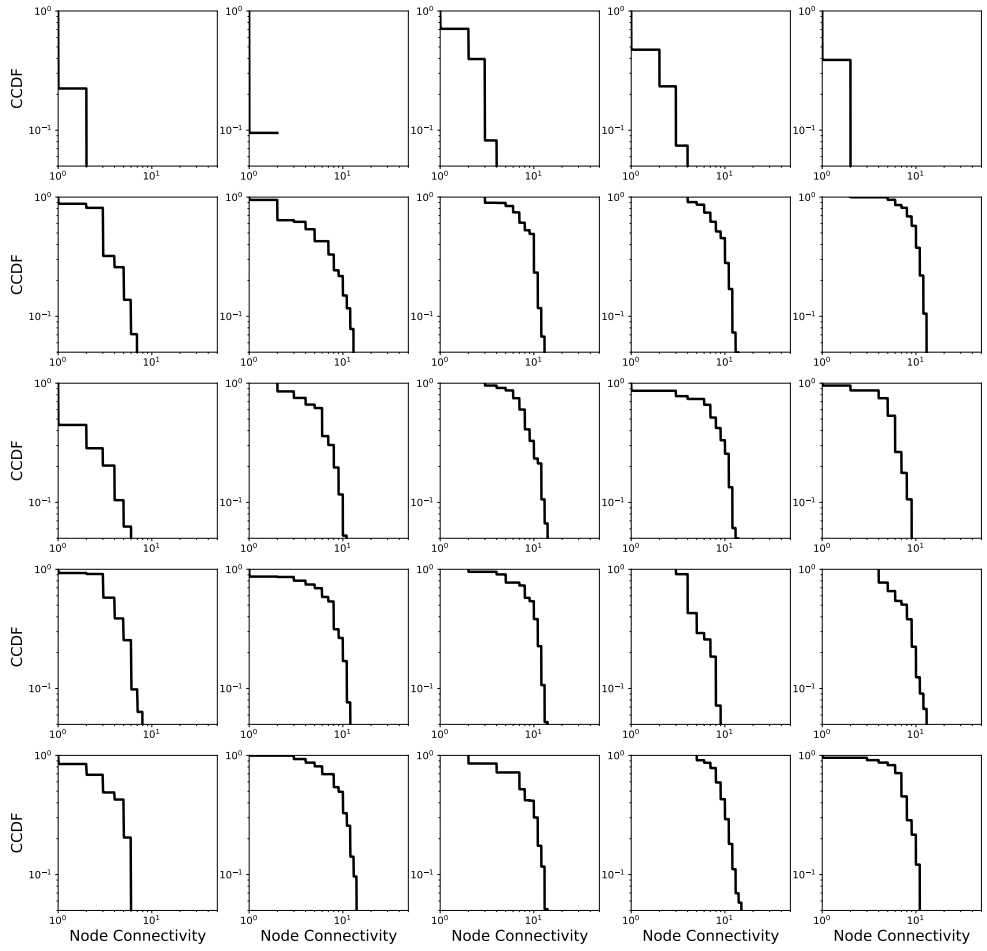

Fig. S9. The node connectivity distributions for networks of each condition $C_{i,j}$, where i (j) indexes the row (column) of the corresponding plot in the grid. These plots are constructed from a single snapshot at quasi-steady state from a trial of each condition.

6. Description of MEDYAN simulation platform

A detailed introduction to the MEDYAN (Mechanochemical Dynamics of Active Networks) model can be found in Ref. 5, and additional extensions and applications of MEDYAN to study the dynamics of actomyosin networks are described in Refs. 6–13. Here we outline the relevant aspects of MEDYAN to facilitate understanding the results in this paper, and direct the reader to the above references for a more thorough description.

A. Simulation protocol. A MEDYAN simulation proceeds by iterating a cycle of four steps which propagate the chemical and mechanical dynamics forward while maintaining a tight coupling between the two. The steps are as follows:

1. Evolve system using stochastic chemical simulation for a time δt.
2. Compute the changes in the mechanical energy resulting from the reactions that occurred in step 1).
3. Mechanically equilibrate the network in response to the new stresses from step 2).
4. Update the reaction rates of force-sensitive reactions based on the new tensions from step 3).

Further details related to these four steps are provided next.

B. Chemistry. In MEDYAN, diffusing chemical species are represented with discrete copy numbers belonging to several compartments, which form a regular grid comprising the simulation volume. The compartment size is chosen so that it may be assumed that inside the compartments the diffusing species are well-mixed, allowing the use of mass-action kinetics to determine their instantaneous propensities to participate in chemical reactions within compartments and diffusion events between adjacent compartments. The minimum Kuramoto length (i.e. the mean free diffusional path length of a reactive species before it participates in a chemical reaction) among the species sets this compartment size to ensure that the well-mixed assumption holds (14). The diffusing chemical species may participate in local chemical reactions according to the copy numbers of the reactants in its compartment, or else they may jump to an adjacent compartment in a diffusion event with a propensity determined by its copy number in the original compartment (15). The algorithm for stochastically choosing which event (including local reactions or jumps between compartments) will occur next is the Next Reaction Method, an accelerated variant of the Gillespie algorithm (15, 16). These are Monte Carlo methods which randomly select both the time to any next event and which event will occur at that time in accordance with each event's instantaneous propensity.

The user specifies the different chemical species and the reactions that they participate in. Several types of reactions are possible. Regular reactions involve only diffusing species (e.g. the conversion of ADP-bound to ATP-bound G-actin monomer). Polymerization reactions result in the subtraction of a diffusing monomer from the local compartment and its conversion into a filament species, and depolymerization reactions do the opposite. Filaments in MEDYAN's have definite spatial coordinates, rather than the compartment-level description of the diffusing species' positions. This network of spatially resolved filaments is overlaid on the compartment grid, so that sections of filaments are able to react with diffusing species according to their local copy numbers. In addition, filaments have mechanical properties which will be discussed in the next section. A filament may react with a diffusing species such as a cross-linker (e.g. α-actinin), branching (e.g. Arp2/3), or molecular motor (e.g. NMIIA). Binding reactions involve a discrete set of binding sites along the filament, and they stochastically occur as chemical reaction events according to the number of those binding sites and the local copy number of diffusing binding molecules. A bound molecular motor may participate in a walking reaction, which causes it to move one of its ends to an adjacent binding site, stretching the motor and generating forces. Other reactions not used in this paper but encompassed by MEDYAN include filament nucleation, filament destruction, filament severing, and filament branching reactions.

C. Mechanics. The mechanical energy U of networks in MEDYAN is a function of the positions of the filament beads and the lengths of the molecules bound to the filaments. There are also potentials describing a branched filament's energy which are not included in this paper. Filament beads mark the joined end points (i.e. hinges) of the cylinders comprising the filament. Individual cylinders can stretch but not bend, but a bending energy term is included for pairs of adjacent cylinders. The energy term for the stretching of cylinders is

$$U_{\text{str}} = \frac{1}{2} K_{\text{fil,str}} (l - l_0)^2, \qquad [1]$$

where $l = ||\mathbf{r}_{i+1} - \mathbf{r}_i||$ is the length of the cylinder whose beads are at positions $\mathbf{r}_{i+1}$ and $\mathbf{r}_i$, l_0 is the cylinder's equilibrium length, and K_{str} is the spring constant of this harmonic potential. The energy term for the bending of adjacent cylinders is

$$U_{\text{bend}} = \epsilon_{\text{bend}} \left(1 - \cos(\theta_{i,i+1})\right), \qquad [2]$$

where ϵ_{bend} parameterizes the strength of the interaction and $\theta_{i,i+1}$ is the angle between the cylinders. Molecules bound to pairs of filaments (e.g. α-actinin and NMIIA) of stretched length l_{bound} have a harmonic stretching energy term:

$$U_{\text{bound,str}} = \frac{1}{2} K_{\text{bound,str}} (l_{\text{bound}} - l^0_{\text{bound}})^2, \qquad [3]$$

where the subscript “bound" indicates that the variables and parameters are specific to the bound molecule. An excluded volume interaction is included to prevent cylinders from overlapping. The analytical formula for this interaction is complicated but can be expressed as a double integral over the two lengths of the participating cylinders i and j:

$$U_{\text{vol},ij} = K_{\text{vol}} \int_0^1 \int_0^1 \frac{dsdt}{||\mathbf{r}_i(s) - \mathbf{r}_j(t)||^4}, \quad [4]$$

where $\mathbf{r}_i(s) = \mathbf{r}_i + s(\mathbf{r}_{i+1} - \mathbf{r}_i)$ is the position along the i cylinder, which is parameterized by a variable s running from 0 to 1 along the cylinder's length. These positions $\mathbf{r}_i(s)$ are also therefore functions of the cylinders' bead positions, $\mathbf{r}_i$ and $\mathbf{r}_{i+1}$. Finally, an exponentially decaying boundary repulsion term prevents the filaments from poking outside the simulation volume:

$$U_{\text{boundary}} = \epsilon_{\text{boundary}} e^{-d_i/\lambda}, \quad [5]$$

where $\epsilon_{\text{boundary}}$ parameterizes the interaction strength, d_i is the distance from the boundary to the nearest endpoint of the i cylinder, and λ parameterizes the interaction screening length.

At the end of each chemical evolution cycle, the positions of the bound molecules and the filament beads will have changed due to the chemical reactions which occurred, displacing the system from near-equilibrium. The positions of the filament beads are then updated in a mechanical equilibration cycle by minimizing the total mechanical energy function U. This is accomplished using the conjugate-gradient minimization algorithm. The minimization procedure ends when the maximum net force remaining in the network is below a user-specified force tolerance F_T, as result of which the system returns to near mechanical equilibrium.

D. Mechanochemical coupling. An important facet of the dynamics of actomyosin networks is that the chemical reaction rates of the associated proteins depend on the forces they sustain: at high tension the myosin minifilaments will walk and unbind more slowly (stalling and catch-bond behavior) whereas the passive cross-linkers are modeled as unbinding more quickly under tension (slip-bond behavior) (17, 18). These force-sensitive behaviors thus play the role of non-linearly coupling the mechanical state of the actomyosin network to its stochastic chemical dynamics.

The myosin motors used in MEDYAN are modeled after non-muscle myosin IIA (NMIIA), which exists in the cell as a minifilament consisting of tens of individual myosin heads. The chemical dynamics of the myosin minifilaments are based on the Parallel Cluster Model of Erdmann et al. (19, 20). In this model, a myosin minifilament contains a number N_{total} of individual myosin heads and has a binding rate to the actin filament pair equal to

$$k_{\text{fil,bind}} = N_{\text{total}} k_{\text{head,bind}}, \quad [6]$$

where $k_{\text{head, bind}}$ is the individual myosin head binding rate. In MEDYAN, N_{total} is uniformly randomly selected between a minimum and maximum number of heads each time a minifilament binds. The bound myosin minifilament has a number of bound heads N^0_{bound} under zero tension equal to the duty ratio ρ times the total number of heads:

$$N^0_{\text{bound}} = \rho N_{\text{total}}. \quad [7]$$

The duty ratio is determined by the individual head unbinding rate:

$$\rho = \frac{k_{\text{head,bind}}}{k^0_{\text{head,unbind}} + k_{\text{head,bind}}}, \quad [8]$$

where $k^0_{\text{head,unbind}}$ is the head unbinding rate under zero tension. Under tension F_{ext} the bound myosin minifilament has altered walking and unbinding rates as well as an altered number of bound heads. The number of bound heads under tension is given by

$$N_{\text{bound}}(F_{\text{ext}}) = \min\left\{N_{\text{total}},\ N^0_{\text{bound}} + \beta \frac{F_{\text{ext}}}{N_{\text{total}}}\right\}, \quad [9]$$

where the parameter $\beta = 2.0$ is chosen to fit experimental data. The myosin minifilament walking rate under zero tension is

$$k^0_{\text{fil,walk}} = s\frac{1-\rho}{\rho} k_{\text{head,bind}}, \quad [10]$$

where s is called the stepping fraction, defined as the ratio of the user-specified real distance between binding sites on the filament d_{step} to the distance between binding sites on the computational cylinder representing the filament segment d_{total}: $s = \frac{d_{\text{step}}}{d_{\text{total}}}$. Equation 10 is based on the PCM and is explained Refs. (5, 19). Under tension, the myosin minifilament walking rate is altered according to a formula of the Hill type:

$$k_{\text{fil,walk}} = \max\left\{0.0,\ k^0_{\text{fil,walk}} \frac{F_{\text{stall}} - F_{\text{ext}}}{F_{\text{stall}} + F_{\text{ext}}/\alpha}\right\}, \quad [11]$$

where the stall force F_{stall} is the maximum tension a minifilament can sustain before it stops walking, and where $\alpha = 0.2$ is another parameter chosen to fit to experimental data. The myosin minifilament will unbind from the pair of actin filaments under zero tension with a rate

$$k^0_{\text{fil,unbind}} = \frac{k_{\text{head,bind}} N_{\text{total}}}{\exp\left(\log\left(\frac{k^0_{\text{head,unbind}} + k_{\text{head,bind}}}{k^0_{\text{head,unbind}}}\right) N_{\text{total}}\right) - 1}. \quad [12]$$

This non-obvious expression is the inverse of the mean residence time of the minifilament as determined using the PCM. Under tension, the myosin minifilament unbinding is modeled with Kramers-type catch-bond behavior:

$$k_{\text{fil,unbind}}(F_{\text{ext}}) = k^0_{\text{fil,unbind}} \max\left\{0.1,\ \exp\left(\frac{-F_{\text{ext}}}{N_{\text{bound}}(F_{\text{ext}}) F_{0,\text{head}}}\right)\right\}, \quad [13]$$

where $F_{0,\text{head}}$ is the characteristic force a single myosin head catch-bond, and the minimum unbinding factor 0.1 is a parameter to chosen to ensure the possibility to unbind under arbitrarily large tension. We assume for myosin minifilaments that the stretching constant is given by

$$K_{\text{bound,str}} = K_{\text{head,str}} N_{\text{bound}}, \quad [14]$$

where $K_{\text{head,str}}$ is the stretching constant for an individual head; this equation assumes the bound heads share the load in parallel.

The unbinding of passive cross-linkers (e.g. α-actinin) are modeled as Kramers-type slip-bond:

$$k_{\text{linker,unbind}}(F_{\text{ext}}) = k^0_{\text{linker,unbind}} \exp\left(\frac{F_{\text{ext}}}{F_{0,\text{linker}}}\right), \quad [15]$$

where $F_{0,\text{linker}}$ is the characteristic force of the cross-linker slip-bond.

Finally, the actin filament will polymerize with a rate that exponentially decreases with the component of the sustained force along the polymerizing tip, F_{ext}. This dependence is based on the Brownian ratchet model of Peskin et al. (21):

$$k_{\text{poly}}(F_{\text{ext}}) = k^0_{\text{poly}} \exp\left(-\frac{F_{\text{ext}}}{F_{0,\text{poly}}}\right), \quad [16]$$

where $F_{0,\text{poly}}$ is the characteristic force of the Brownian ratchet model, and k^0_{poly} is the zero-force polymerization rate.

Any of the above characteristic forces F_0 may be converted to a corresponding characteristic distance x_0 via

$$F_0 = k_B T / x_0, \quad [17]$$

where $k_B T$ is the thermal energy, casting expressions of the form F_{ext}/F_0 to the form $F_{\text{ext}} x_0 / k_B T$.

E. Parameterization. The following table lists the parameters chosen for the simulations presented in this paper.

Parameter	Description	Value
	General Simulation Parameters	
k_BT	Thermal energy	$4.1\ pN \cdot nm$
L_{comp}	Cubic compartment side length	$500\ nm$
$N_x,\ N_y,\ N_z$	Number of compartments in each dimension	$2,\ 2,\ 2$
L_{cyl}	Filament cylinder equilibrium length	$54\ nm$
δt	Length of chemical evolution step	$0.05\ s$
F_T	Force tolerance of mechanical minimization	$1\ pN$
	Mechanical Parameters	
$K_{\text{fil,str}}$	Actin filament stretching constant	$100\ pN/nm$ (5)
ϵ_{bend}	Actin filament bending energy	$1344\ pN \cdot nm$ (5, 22)
K_{vol}	Cylinder excluded volume constant	$10^5\ pN/nm^4$ (5)
$K_{\text{head,str}}$	NMIIA head stretching constant	$2.5\ pN/nm$ (23)
$K_{\alpha,\text{str}}$	α-actinin stretching constant	$8\ pN/nm$ (24)
$\epsilon_{\text{boundary}}$	Boundary repulsion energy	$41\ pN \cdot nm$ [a]
λ	Boundary repulsion screening length	$2.7\ nm$ [b]
	Mechanochemical Parameters	
$N_{\text{NMIIA,bind}}$	Binding sites per cylinder for myosin motors	8 [c]
$N_{\alpha,\text{bind}}$	Binding sites per cylinder for α-actinin	4 [d]
d_{step}	NMIIA minifilament step size	$6.0\ nm$ (23)
$N_{\text{min}},\ N_{\text{max}}$	Range of number of NMIIA heads per minifilament	$15,\ 25$ [e] (25)
F_{stall}	Stall force of NMIIA minifilament	$100\ pN$ [f]
$F_{0,\text{head}}$	Characteristic force of NMIIA catch-bond	$12.6\ pN$ (19)
$F_{0,\alpha}$	Characteristic force of α-actinin slip-bond	$17.2\ pN$ (26)
$F_{0,\text{poly}}$	Characteristic force of actin Brownian ratchet	$1.5\ pN$ (27)
l_M	Equilibrium length of NMIIA minfilament	$175 - 225\ nm$ (5)
l_α	Equilibrium length of α-actinin	$30 - 40\ nm$ (5)
	Chemical Parameters	
$k_{\text{actin,diff}}$	Diffusion constant of actin monomer	$20\ \mu M s^{-1}$ (5)
$k_{\alpha,\text{diff}}$	Diffusion constant of α-actinin	$2\ \mu M s^{-1}$ (5, 28)
$k_{\text{motor,diff}}$	Diffusion constant of NMIIA minifilament	$0.2\ \mu M s^{-1}$ (5)
$k_{\text{actin,poly,+}}$	Actin plus-end polymerization	$11.6\ \mu M s^{-1}$ (29)
$k_{\text{actin,poly,-}}$	Actin minus-end polymerization	$1.3\ \mu M s^{-1}$ (29)
$k_{\text{actin,depoly,+}}$	Actin plus-end depolymerization	$1.4\ s^{-1}$ (29)
$k_{\text{actin,depoly,-}}$	Actin minus-end depolymerization	$0.8\ s^{-1}$ (29)
$k_{\text{head,bind}}$	NMIIA head binding	$0.2\ s^{-1}$ (30)
$k^0_{\text{head,unbind}}$	NMIIA head unbinding under zero tension	$1.7\ s^{-1}$ (5, 30)
$k_{\alpha,\text{bind}}$	α-actinin binding	$0.7\ \mu M s^{-1}$ (31)
$k^0_{\alpha,\text{unbind}}$	α-actinin unbinding under zero tension	$0.3\ s^{-1}$ (31)

Table S1. All parameters used in the simulations reported in this paper.

[a] - Chosen for the energy scale to be 10 k_BT.

[b] - Chosen as the the length of a G-actin monomer.

[c] - Chosen to allow the spacing between binding sites to be roughly equal to its physiological value near 6 nm (23).

[d] - Chosen to allow the spacing between binding sites to be roughly equal to its physiological value near 30 nm (32).

[e] - Chosen to given an average $N_{\text{total}} = 20$ in approximate agreement with literature values (25).

[f] - A wide range of values are found in the literature for the stall force of the minifilament. We take an order of magnitude estimate for this parameter based on the stall force of a single head (on the order of 10 pN, estimated as $d_{\text{step}}K_{\text{head,str}}$ (5)) times the number of bound heads in the minifilament (on the order of 10). This parameter choice is empirically valid as it yields observable network contraction.

7. Dependence on δt and F_T

The heavy-tailed distributions of $|\Delta U_-|$, the magnitudes of the negative energy increments which are the chief subject of this paper, may have strong dependence on certain key parameters governing the mechanical equilibration protocol. To ensure that these distributions are not artifacts of simulation we investigate whether changing the parameters F_T and δt alters the qualitative properties of the distributions. In Figure S10 we compare these distributions using 3 runs for each parameter choice. Only weak dependence on F_T is observed (Figure S10.A). We find strong dependence on δt (Figure S10.B), however for each parameter choice heavy tails exist and thus we may conclude that the cytoquake phenomenon is not an artifact despite their frequency and magnitude having dependence on δt. We can ask whether the observed discrepancy between the distributions

for different choices of δt is due to a change in the underlying dynamics or due to the effect of summing over larger time intervals to obtain the quantities ΔU. We expect that by summing over larger time intervals, the heavy tails are "averaged out," or coarse-grained, causing them to be increasingly Gaussian for larger δt. We can check this by summing consecutive increments ΔU for small choices of δt over time windows equal to the largest value of δt tested. When this is done (shown in Figure S10.C), we find the distributions for all choices of δt to approximately collapse on each other. This suggests that coarse-graining in time indeed explains the discrepancy in the distributions of $|\Delta U|_-$ in Figure S10.B. Without showing the data, we find a similar picture to apply for the distributions of positive increments ΔU_+, with a similar asymmetry in the non-Gaussian parameters for all choices of δt and F_T as observed for conditions used in main text, $\delta t = 0.05\ s$ and $F_T = 1\ pN$. While a smaller choice for F_T and δt should correspond more closely to reality, we find that for the smallest of the tested values for these parameters the simulations did not complete in the allotted computer wall time of 2 weeks. Thus our choices for these parameters used in this paper are chosen to be small while still allowing us to run full 2,000 s simulations.

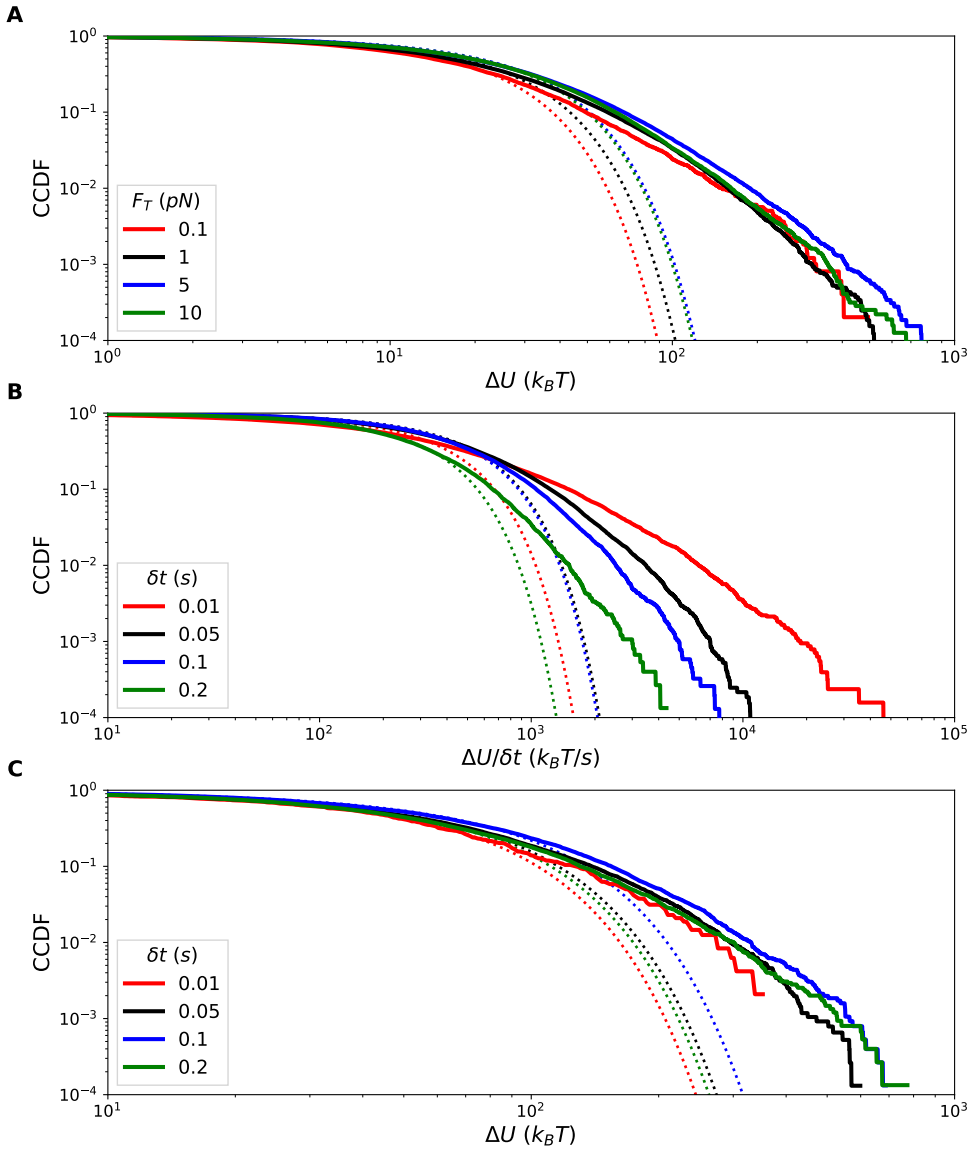

Fig. S10. A: Complementary cumulative distribution functions of the negative increments $|\Delta U_-|$ at QSS for various choices of the force tolerance parameter F_T plotted against fitted half-normal CCDFs. For these runs condition $C_{3,3}$ is used with $\delta t = 0.05\ s$. **B**: CCDFs of the negative increments $|\Delta U_-|$ at QSS for various choices of the time between minimization, δt. The energy increments are normalized by δt for more direct comparison between these curves. For these runs condition $C_{3,3}$ is used with $F_T = 2\ pN$. **B**: Complementary cumulative distribution functions of the negative increments $|\Delta U_-|$ at QSS for various choices of the time between minimization, δt. The energy increments are normalized by δt for more direct comparison between these curves. For these runs condition $C_{3,3}$ is used with $F_T = 1\ pN$. **C**: The same data is shown as in part **B**, except here ΔU for each choice of δt is obtained by summing consecutive energy increments over time windows equal to $0.2\ s$. In this way the values of ΔU for each choice of δt correspond to the same duration of time.

We also investigated how the fraction of negative eigenvalues persisting after mechanical minimization depends on the force threshold F_T. When minimization ceases at higher forces, more negative eigenvalues are left remaining, as expected. This behavior is illustrated in Figure S11.

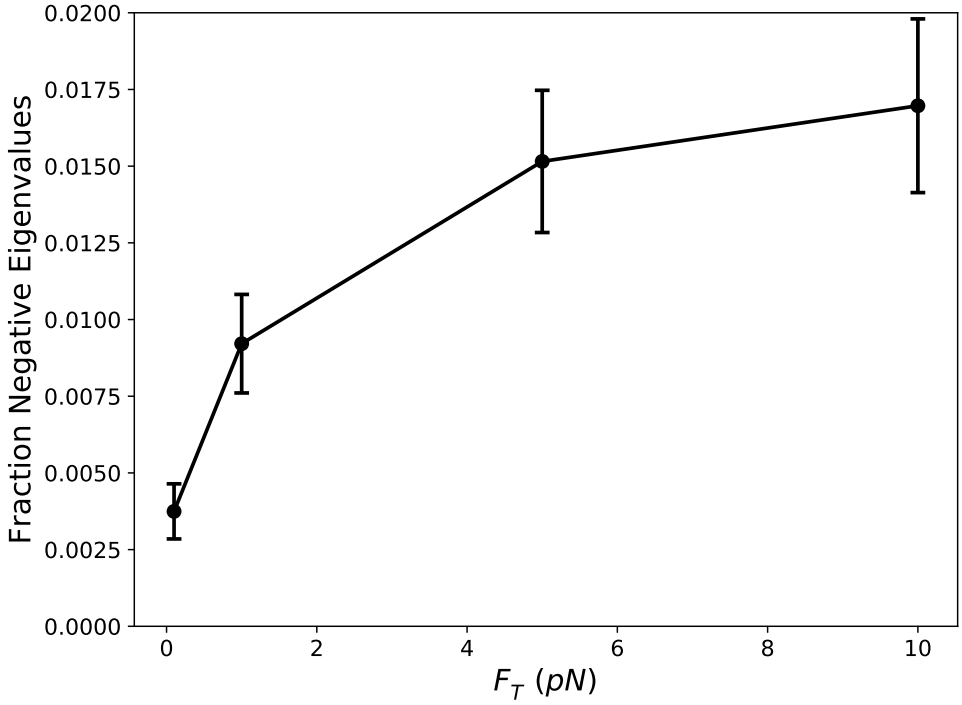

Fig. S11. Scatter plot showing the fraction of negative eigenvalues remaining after mechanical minimization when different choices of the parameter F_T are used. The data is collected from QSS for 3 runs of $C_{3,3}$, with the standard deviation taken over time and over the runs.

8. Machine learning model

A. Cytoquake classification. To forecast the occurrence of cytoquakes, we resorted to using a high-dimensional ML model (3 layer feed-forward neural network) after it was found that several simple features in the eigenspectrum which we believed might reflect mechanical stability (for instance the value of the smallest positive eigenvalue) did not by themselves significantly correlate with cytoquake occurrence. We pose the forecasting of cytoquakes as a binary classification problem. A trajectory $\Delta U(t) = U(t+\delta t) - U(t)$ at QSS (after 1,000 s) is converted to a binary sequence such that each t for which $\Delta U(t) \leq \Delta U_T$, as well as the $t_W = 0.15$ previous seconds (i.e. 3 previous time points) are classified as cytoquakes, and the rest are not. This t_W window is chosen to help overcome the stochasticity inherent in the chemical dynamics which, along with the instantaneous mechanical stability we are using as a predictor, controls cytoquake occurrence. We focus here on the five runs of conditions $C_{3,3}$. $\Delta U_T = -100\ k_B T$ is chosen to lie well in the tail of the distribution of $|\Delta U_-|$ for this condition and therefore distinguishes rare events, as shown in Figure 1 in the main text. With these choices, $\sim 10\%$ of samples across all runs are labeled as events in the classification problem.

B. Model inputs. The predictors of the model capture information about the network's mechanical stability. The ordered sets of eigenvalues $\{\lambda_k\}_{k=1}^{3N}$ at each time t is padded by adding zero eigenvalues between the unstable ($\lambda_k < 0$) and stable ($\lambda_k \geq 0$) parts of the spectrum to maintain a fixed input dimension across all time points and runs. We then collect these eigenvalues into a tuple $\mathbf{M}(t)$ such that the first element of $\mathbf{M}(t)$ is the largest negative λ_k at time t and the last element is the largest positive λ_k at time t. We optionally include the the inverse participation ratios $\{r_k\}_{k=1}^{3N}$ in this vector by first adding zeros in the places of the set $\{r_k\}_{k=1}^{3N}$ corresponding to where zeros were added in the set $\{\lambda_k\}_{k=1}^{3N}$, and then interleaving the λ_k and r_k in the now doubly sized tuple $\mathbf{M}(t)$, so that now for example the first two elements of $\mathbf{M}(t)$ correspond to the largest negative λ_k and the associated r_k at time t. The tuples $\mathbf{M}(t)$ are then linearly rescaled, so for each element $M_i(t)$ the average over all times of a run is 0 and the variance is 1. These rescaled tuples are labeled $\widetilde{\mathbf{M}}(t)$.

When only the λ_k are included then $\widetilde{\mathbf{M}}(t)$ has $\sim$ 1,600 dimensions, and with the r_k are also included it has $\sim$ 3,200 dimensions. To avoid overfitting the model, we first reduce the dimensionality of $\widetilde{\mathbf{M}}(t)$ via principal component analysis (PCA) using all QSS time points in a run. We choose 30 dimensions as the size of the reduced tuple $\mathbf{m}(t)$ because this allows for more than 95% of the variance of $\widetilde{\mathbf{M}}(t)$ to be explained when just the λ_k are included as shown in Figure S12.A. Model performance appreciably decreases when fewer than 30 dimension are used and improves only marginally if more are used. A row of ones is added as a 31^{st} dimension to $\mathbf{m}(t)$ as a bias for the neural network. As an additional indicator of the network's mechanical stability we also consider its mechanical energy U at time t. $U(t)$ is linearly rescaled to give $\widetilde{U}(t)$ so that it has zero mean and unit variance. We then optionally augment with input tuple $\mathbf{m}(t)$ with the $\widetilde{U}(t)$ as a 32^{nd} dimension.

C. Treating multiple trials. We can treat the data from all five runs of condition $C_{3,3}$ separately or combine all data together to train a larger model. Model performance is generally found to be better when trained on data from a single run, however by combining data from all runs we probe more general underlying trends that are not specific to the network organization of one run. When describing trends from varying model inputs, as in Figure S12.D, we focus on results obtained by combining all runs due to their greater generality.

For a single run there are $\sim$ 20,000 samples, giving 100,000 samples when combining all runs. When combining runs, we first rescale and perform PCA on the predictors using only the data within a single run, and then concatenate the resulting $\mathbf{m}(t)$ with their associated labels into a larger data set. This way the relative variation of the predictors compared to their typical values for a particular organization of the actomyosin network is retained, and the typical values of particular network organizations themselves affect the model inputs to a lesser degree.

D. Neural network architecture. We used the Python modules scikit-learn and Keras with a Tensorflow back end to train a deep feed-forward neural network and a logistic regression model for the binary classification problem (33, 34). The 31 or 32-dimensional (depending on if $\widetilde{U}(t)$ is included as a predictor) input tuple $\mathbf{m}$ is fed into three fully connected hidden layers L_i, $i = 1, 2, 3$, each with either 30 or 100 nodes depending on if the data consists of a single run (20,000 samples) or of all five runs (100,000 samples). Each node in the hidden layers uses a rectified linear unit activation function. The output of the network is two nodes using a softmax activation function whose values are p and $1-p$, where p is the predicted probability of a cytoquake event at that time t. This architecture is schematically illustrated in Figure S12.B. The network is trained for either 400 or 200 epochs using a categorical cross-entropy loss function with Adam optimization in stochastically chosen batches of either 1,000 or 10,000 samples, depending on the whether the single or multiple run data sets, respectively, are used. The cytoquake samples are given a higher weight ($\times 3$) than the non-cytoquake samples during training. A L2 penalty of 0.05 is used to curb overfitting. When using only $\widetilde{U}(t)$ as a predictor, a logistic regression model is fit using the same sample weights.

E. Model validation. Of all the data samples, we use 2/3 to train the model with and validate the model on the remaining 1/3. We repeat these random training/testing set splits to gather statistics on model performance. The binary classification procedure involves the probability threshold p_T (such that $p > p_T$ means the model predicts a cytoquake). Model performance is measured by varying p_T from 0 to 1 and measuring the true positive rate (TPR, the proportion of actual cytoquakes correctly predicted as such) and false positive rate (FPR, the proportion of actual non-cytoquakes incorrectly predicted as cytoquakes) on the test data; the locus of these points forms the receiver operator characteristic (ROC) curve. A random model would have

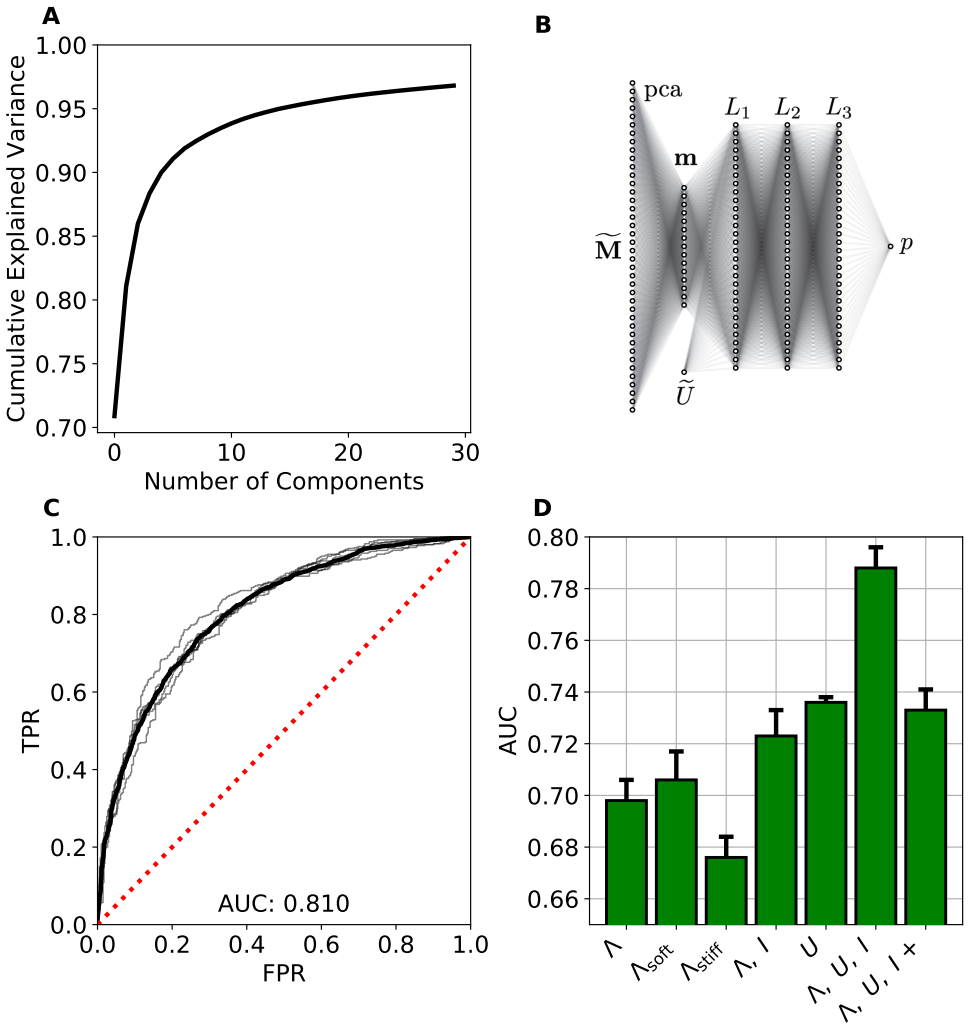

Fig. S12. **A**: Cumulative explained variance from PCA of the $\sim 1,600$ eigenvalues $\{\lambda_k(t)\}_{k=1}^{3N}$. **B**: Schematic depiction of the feed-forward neural network architecture. **C**: ROC curves for the model using only $\{\lambda_k\}_{k=1}^{3N}$ as input and trained on a single run of condition $C_{3,3}$, with five realizations of the stochastic batch network training and their average shown. The ROC curve of a random model is plotted as the red dotted line. **D**: Bar plot indicating the AUC of ROC curves using different combinations of inputs for the model trained on data collected from all runs of condition $C_{3,3}$. From left to right, the labels indicate that the model inputs are: $\{\lambda_k\}_{k=1}^{3N}$; $\{\lambda_k | 0 \leq \lambda_k < \lambda_T\}$; $\{\lambda_k | \lambda_T \leq \lambda_k\}$; $\{\lambda_k\}_{k=1}^{3N}$ and $\{r_k\}_{k=1}^{3N}$; U, using a logistic regression model; $\{\lambda_k\}_{k=1}^{3N}$, $\{r_k\}_{k=1}^{3N}$, and U; $\{\lambda_k\}_{k=1}^{3N}$, $\{r_k\}_{k=1}^{3N}$, and U with forecasting done for large positive increments $\Delta U > 100\ k_B T$. Error bars indicate uncertainty from five realizations of stochastic batch training.

FPR = TPR, so an area under the curve (AUC) of the ROC curve greater than 0.5 indicates a good model, and a perfect model would have an AUC of 1. One can also consider precision-recall (PR) curves, which contain points in the space of model precision (the proportion of predicted cytoquakes which were actual cytoquakes) and recall (the same as TPR). A random model would have the same precision, equal to the proportion of actual cytoquakes in the testing data, for all values of recall as p_T is varied, giving an AUC equal to that proportion.

When the test data is unbalanced, i.e. when there are many more non-cytoquake events than cytoquake events, it has been shown that the AUC of the PR curve is a more faithful metric for model performance (since a model may score a high AUC of the ROC curve by overestimating that events are not cytoquakes) (35, 36). To overcome this limitation of ROC curves, which we believe has a more intuitive interpretation that PR curves, we balance the testing data, keeping all cytoquake events and randomly keeping an equal number of non-cytoquake events. We confirmed that trends observed in the AUC of the ROC curves as the model is varied also hold when considering the AUC of PR curves on the full test set.

In Figure S13 we show examples of these PR and ROC curves on the training and testing data for a model trained on a single run. The very high AUC of the PR and ROC curves evaluated on the training data indicates that the model has nearly perfected its prediction on those samples and may indicate overfitting, however this high performance generalizes nicely to the unseen testing data. Note that the AUC of the ROC evaluated on the testing data is significantly higher than shown in Figure S12.D reflecting the generally higher performance of models trained on data from a single run compared to models trained on data from all runs.

Finally, as a sanity check, we confirmed that randomly shuffling the labels on the training set decreases performance on the training set and causes the performance on the test set to decrease to that of a random model, as shown in Figure S14.

F. Varying the machine learning model inputs. Applying the model using the Hessian eigenspectrum as the input, we obtained an AUC of 0.81 when using data from a single run of condition $C_{3,3}$ (Figure S12.C) and of 0.70 when using data from five runs, i.e. from five different network realizations. In Figure S12.D, we display the effects of varying the machine learning model inputs on prediction performance, reflecting the degree to which cytoquake occurrence depends on the various inputs. We point out that these trends from varying the model inputs are not particularly strong, contributing only marginal changes (though greater the measured uncertainty) to the model performance. These differences are less than the difference resulting from combing all five runs in a data set rather than using one run. We report them here mainly out of completeness, rather than in support of some strong conclusion.

Uncertainty in AUC from five repetitions of stochastic batch training is roughly 0.01 for all reported values. Keeping only the eigenvalues of the soft modes does not harm performance (AUC 0.71), while keeping only the stiff modes does harm performance (AUC 0.68). Performance is not harmed (AUC 0.72) upon augmenting the input with the inverse participation ratios $\{r_k(t)\}_{k=1}^{3N}$. Interestingly, we found that a logistic regression model using only the mechanical energy $U(t)$ as an input feature performs well (AUC 0.74, with a smaller uncertainty around 0.002 for this simpler model), reminiscent of the debate concerning one neuron vs. deep learning models of earthquake aftershock prediction (37, 38). This logistic regression model has learned an optimal cutoff for U that indicates instability and likely cytoquake occurrence. We may seemingly conclude that the machine learning model using the Hessian eigenspectrum as an input has merely learned what the mechanical energy is, however we find that by far the best performance results from combining $\{\lambda_k(t)\}_{k=1}^{3N}$, $\{r_k(t)\}_{k=1}^{3N}$, and $U(t)$ in the ML model, reaching an AUC of 0.79 when using data from all five runs. This suggests that the learned features of the Hessian eigenspectrum are not redundant given U, i.e. that their mutual information is low. Finally, we found that prediction of large positive increments ($\Delta U > 100\ k_B T$) is also possible, with an AUC of 0.74 when combining all inputs.

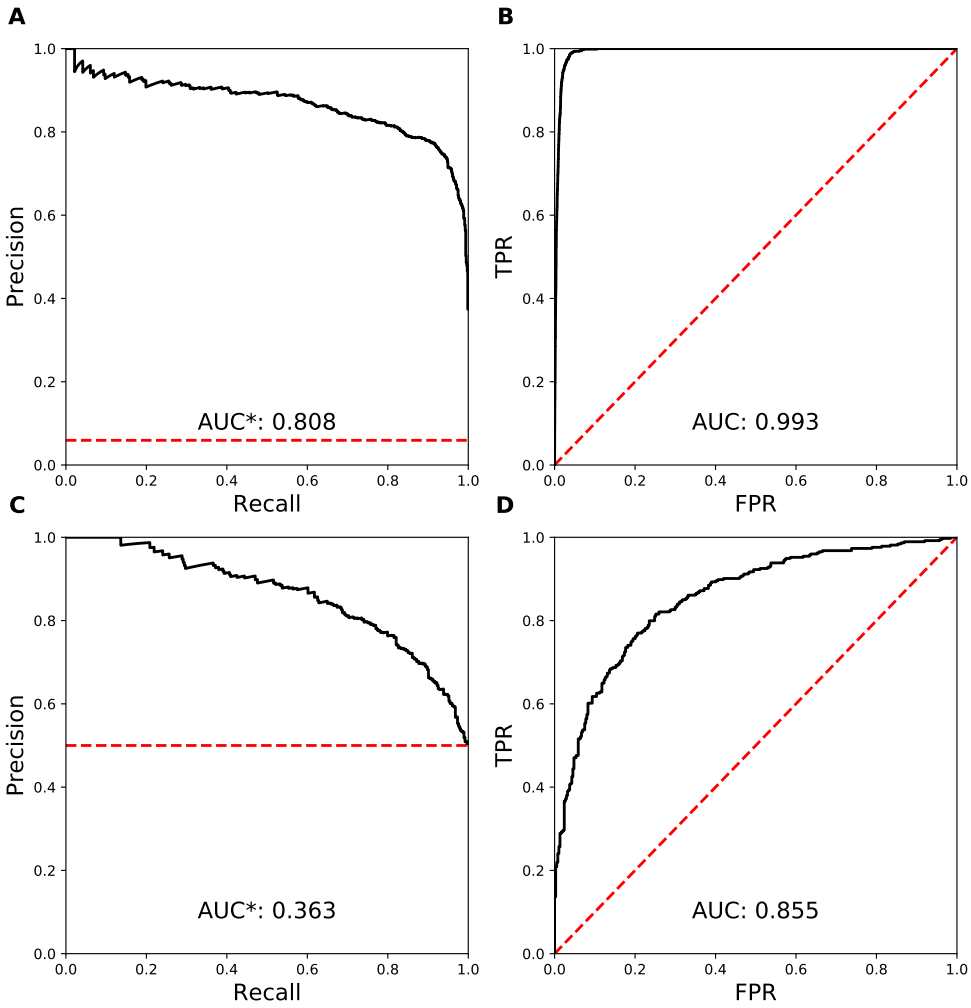

Fig. S13. **A**: PR curve evaluated for a model using $\{\lambda_k\}_{k=1}^{3N}$, $\{r_k\}_{k=1}^{3N}$, and U as inputs trained on data from a single run at QSS of condition $C_{3,3}$ and evaluated on the training data. The red line indicates the performance of a random model on the data set. The asterisk on the AUC indicates that the fraction of cytoquake samples in the data set (for this run ~ 0.06) has been subtracted from the actual AUC, to give the area between the black and red curves. **B**: ROC curve for the same model evaluated on the training data. **C**: PR curve for the same model evaluated on the balanced testing data. **D**: ROC curve for the same model evaluated on the balanced testing data.

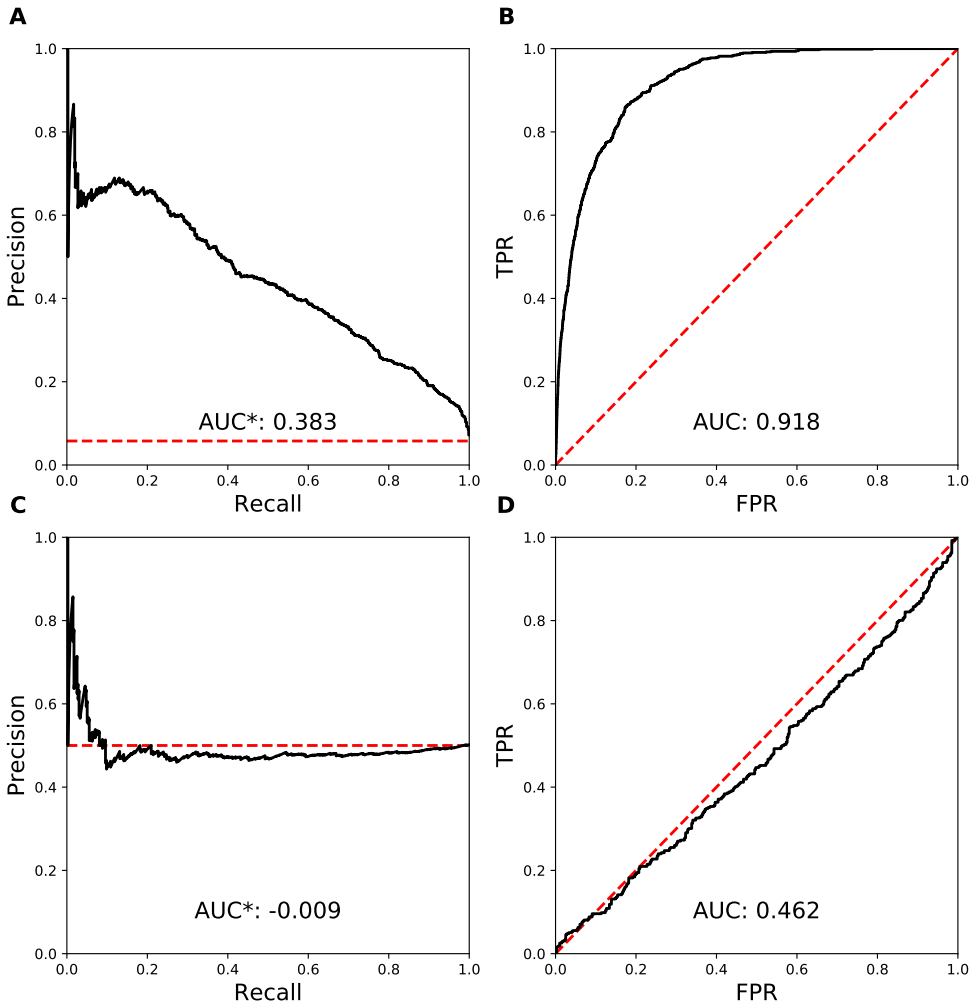

Fig. S14. A: PR curve evaluated for a model using $\{\lambda_k\}_{k=1}^{3N}$, $\{r_k\}_{k=1}^{3N}$, and U as inputs trained on data from a single run at QSS of condition $C_{3,3}$ and evaluated on the training data, when the training data labels have been randomly shuffled. The red line indicates the performance of a random model on the data set. **B**: ROC curve for the same model evaluated on the training data. **C**: PR curve for the same model evaluated on the balanced testing data. **D**: ROC curve for the same model evaluated on the balanced testing data.

Movie S1. The movie SIMovie1(C33Trajectory).mp4 is a visualization of a 2,000 s long MEDYAN trajectory of cytoskeletal self-organization for the experimental condition $C_{3,3}$, which is described in the main text.

Movie S2. The movie SIMovie2(C31_100.11).mp4 is a visualization of a vibrational normal mode corresponding to eigenvalue $100.11/pN/nm$ for experimental condition $C_{3,1}$. The amplitude of the oscillation is chosen to allow easy visualization and is not to scale with any physical quantity.

Movie S3. The movie SIMovie3(C33_0.66).mp4 is a visualization of a vibrational normal mode corresponding to eigenvalue $100.11/pN/nm$ for experimental condition $C_{3,3}$. The amplitude of the oscillation is chosen to allow easy visualization and is not to scale with any physical quantity.

Movie S4. The movie SIMovie4(C33_5.83).mp4 is a visualization of a vibrational normal mode corresponding to eigenvalue $5.83/pN/nm$ for experimental condition $C_{3,3}$. The amplitude of the oscillation is chosen to allow easy visualization and is not to scale with any physical quantity.

Movie S5. The movie SIMovie5(C33_13.75).mp4 is a visualization of a vibrational normal mode corresponding to eigenvalue $13.75/pN/nm$ for experimental condition $C_{3,3}$. The amplitude of the oscillation is chosen to allow easy visualization and is not to scale with any physical quantity.

References

1. DN Prabhakar Murthy, Min Xie, and Renyan Jiang. *Weibull models*, volume 505. John Wiley & Sons, 2004.
2. David N Reshef, Yakir A Reshef, Hilary K Finucane, Sharon R Grossman, Gilean McVean, Peter J Turnbaugh, Eric S Lander, Michael Mitzenmacher, and Pardis C Sabeti. Detecting novel associations in large data sets. *science*, 334(6062): 1518–1524, 2011.
3. Robert V Hogg, Joseph McKean, and Allen T Craig. *Introduction to mathematical statistics*. Pearson Education, 2005.
4. José Alvarado, Michael Sheinman, Abhinav Sharma, Fred C MacKintosh, and Gijsje H Koenderink. Molecular motors robustly drive active gels to a critically connected state. *Nature Physics*, 9(9):591–597, 2013.
5. Konstantin Popov, James Komianos, and Garegin A Papoian. Medyan: mechanochemical simulations of contraction and polarity alignment in actomyosin networks. *PLoS computational biology*, 12(4), 2016.
6. Carlos Floyd, Garegin A Papoian, and Christopher Jarzynski. Quantifying dissipation in actomyosin networks. *Interface focus*, 9(3):20180078, 2019.
7. Aravind Chandrasekaran, Arpita Upadhyaya, and Garegin A Papoian. Remarkable structural transformations of actin bundles are driven by their initial polarity, motor activity, crosslinking, and filament treadmilling. *PLoS computational biology*, 15(7), 2019.
8. James E Komianos and Garegin A Papoian. Stochastic ratcheting on a funneled energy landscape is necessary for highly efficient contractility of actomyosin force dipoles. *Physical Review X*, 8(2):021006, 2018.
9. Qin Ni and Garegin A Papoian. Turnover versus treadmilling in actin network assembly and remodeling. *Cytoskeleton*, 2019.
10. Xiaona Li, Qin Ni, Xiuxiu He, Jun Kong, Soon-Mi Lim, Garegin A Papoian, Jerome P Trzeciakowski, Andreea Trache, and Yi Jiang. Tensile force induced cytoskeletal reorganization: Mechanics before chemistry. *BioRxiv*, 2020.
11. Carlos Floyd, Garegin A Papoian, and Christopher Jarzynski. Gibbs free energy change of a discrete chemical reaction event. *The Journal of Chemical Physics*, 152(8):084116, 2020.
12. Haoran Ni and Garegin A Papoian. Membrane-medyan: Simulating deformable vesicles containing complex cytoskeletal networks. *bioRxiv*, 2021.
13. Carlos Floyd, Aravind Chandresekaran, Haoran Ni, Qin Ni, and Garegin A Papoian. Segmental lennard-jones interactions for semi-flexible polymer networks. *Molecular Physics*, page e1910358, 2021.
14. Olaf Wolkenhauer, Peter Wellstead, Kwang-Hyun Cho, Ramon Grima, and Santiago Schnell. Modelling reaction kinetics inside cells. *Essays in biochemistry*, 45:41–56, 2008.
15. David Bernstein. Simulating mesoscopic reaction-diffusion systems using the gillespie algorithm. *Physical Review E*, 71(4): 041103, 2005.
16. Daniel T Gillespie. Exact stochastic simulation of coupled chemical reactions. *The journal of physical chemistry*, 81(25): 2340–2361, 1977.
17. David Keller and Carlos Bustamante. The mechanochemistry of molecular motors. *Biophysical journal*, 78(2):541–556, 2000.
18. Yuriy V Pereverzev, Oleg V Prezhdo, Manu Forero, Evgeni V Sokurenko, and Wendy E Thomas. The two-pathway model for the catch-slip transition in biological adhesion. *Biophysical journal*, 89(3):1446–1454, 2005.
19. Thorsten Erdmann, Philipp J Albert, and Ulrich S Schwarz. Stochastic dynamics of small ensembles of non-processive molecular motors: The parallel cluster model. *The Journal of chemical physics*, 139(17):11B604_1, 2013.
20. Thorsten Erdmann, Kathrin Bartelheimer, and Ulrich S Schwarz. Sensitivity of small myosin ii ensembles from different isoforms to mechanical load and atp concentration. *Physical Review E*, 94(5):052403, 2016.

21. Charles S Peskin, Garrett M Odell, and George F Oster. Cellular motions and thermal fluctuations: the brownian ratchet. *Biophysical journal*, 65(1):316–324, 1993.
22. A Ott, M Magnasco, A Simon, and A Libchaber. Measurement of the persistence length of polymerized actin using fluorescence microscopy. *Physical Review E*, 48(3):R1642, 1993.
23. Andrej Vilfan and Thomas Duke. Instabilities in the transient response of muscle. *Biophysical Journal*, 85(2):818–827, 2003.
24. BA DiDonna and Alex J Levine. Unfolding cross-linkers as rheology regulators in f-actin networks. *Physical Review E*, 75 (4):041909, 2007.
25. Neil Billington, Aibing Wang, Jian Mao, Robert S Adelstein, and James R Sellers. Characterization of three full-length human nonmuscle myosin ii paralogs. *Journal of Biological Chemistry*, 288(46):33398–33410, 2013.
26. Jorge M Ferrer, Hyungsuk Lee, Jiong Chen, Benjamin Pelz, Fumihiko Nakamura, Roger D Kamm, and Matthew J Lang. Measuring molecular rupture forces between single actin filaments and actin-binding proteins. *Proceedings of the National Academy of Sciences*, 105(27):9221–9226, 2008.
27. Matthew J Footer, Jacob WJ Kerssemakers, Julie A Theriot, and Marileen Dogterom. Direct measurement of force generation by actin filament polymerization using an optical trap. *Proceedings of the National Academy of Sciences*, 104 (7):2181–2186, 2007.
28. Longhua Hu and Garegin A Papoian. Mechano-chemical feedbacks regulate actin mesh growth in lamellipodial protrusions. *Biophysical journal*, 98(8):1375–1384, 2010.
29. Ikuko Fujiwara, Dimitrios Vavylonis, and Thomas D Pollard. Polymerization kinetics of adp-and adp-pi-actin determined by fluorescence microscopy. *Proceedings of the National Academy of Sciences*, 104(21):8827–8832, 2007.
30. Mihály Kovács, Fei Wang, Aihua Hu, Yue Zhang, and James R Sellers. Functional divergence of human cytoplasmic myosin ii kinetic characterization of the non-muscle iia isoform. *Journal of Biological Chemistry*, 278(40):38132–38140, 2003.
31. Daniel H Wachsstock, WH Schwartz, and Thomas D Pollard. Affinity of alpha-actinin for actin determines the structure and mechanical properties of actin filament gels. *Biophysical journal*, 65(1):205, 1993.
32. Rudolf K Meyer and Ueli Aebi. Bundling of actin filaments by alpha-actinin depends on its molecular length. *The Journal of cell biology*, 110(6):2013–2024, 1990.
33. François Chollet et al. Keras. https://keras.io, 2015.
34. F. Pedregosa, G. Varoquaux, A. Gramfort, V. Michel, B. Thirion, O. Grisel, M. Blondel, P. Prettenhofer, R. Weiss, V. Dubourg, J. Vanderplas, A. Passos, D. Cournapeau, M. Brucher, M. Perrot, and E. Duchesnay. Scikit-learn: Machine learning in Python. *Journal of Machine Learning Research*, 12:2825–2830, 2011.
35. Jesse Davis and Mark Goadrich. The relationship between precision-recall and roc curves. In *Proceedings of the 23rd international conference on Machine learning*, pages 233–240, 2006.
36. Takaya Saito and Marc Rehmsmeier. The precision-recall plot is more informative than the roc plot when evaluating binary classifiers on imbalanced datasets. *PloS one*, 10(3), 2015.
37. Phoebe MR DeVries, Fernanda Viégas, Martin Wattenberg, and Brendan J Meade. Deep learning of aftershock patterns following large earthquakes. *Nature*, 560(7720):632–634, 2018.
38. Arnaud Mignan and Marco Broccardo. One neuron versus deep learning in aftershock prediction. *Nature*, 574(7776): E1–E3, 2019.